ACCSCIENCE PUBLISHING

Materials Science in Additive Manufacturing

ORIGINAL RESEARCH ARTICLE

Optimizing 3D printing parameters for lightweight and high-strength unmanned aerial vehicle parts

Saleem Ramadan[1†*] and Mohammad Abu-Shams[2†]

[1]Department of Industrial Engineering, School of Engineering Technology, Al Hussein Technical University, Amman, Jordan

[2]Department of Industrial Engineering, School of Applied Technical Sciences, German Jordanian University, Amman, Jordan

Abstract

Additive manufacturing, particularly fused deposition modelling (FDM), has gained increasing attention in aerospace applications due to its capability to produce complex geometries with reduced material usage, making it a promising approach for manufacturing lightweight yet strong unmanned aerial vehicle (UAV) parts. In this study, an integrated framework was developed to optimize FDM parameters for producing UAV parts that are both lightweight and high in strength. A response surface methodology was used to analyze the effects of infill percentage, layer height, number of walls, and build plate temperature on the mass and tensile strength of the printed parts. Two regression models with high predictive accuracy were constructed (R^2 = 98.2% for mass, R^2 = 88.5% for tensile strength). A multi-objective optimization approach was applied, using the non-dominated sorting genetic algorithm II Pareto front analysis in combination with Minitab's Response Optimizer tool, to identify the optimal combination of parameters. The results showed that layer height, number of walls, and infill percentage, along with their interaction effects and quadratic effects, had the most significant effects on both mass and tensile strength, whereas build plate temperature had negligible effects. The results from the Pareto front analysis revealed the trade-off between minimizing mass and maximizing tensile strength for the parts. The optimal parameter settings (e.g., 58.26% infill percentage, 0.1635-mm layer height, 4 walls, and 65°C build plate temperature) achieved a tensile strength of 47.08 MPa and a mass of 1.60 g, offering a well-balanced strength-to-weight ratio suitable for UAV applications.

Keywords: Fused deposition modeling; Unmanned aerial vehicle parts; Multi-objective optimization; Response surface methodology; Tensile strength; 3D printing parameters

[†]These authors contributed equally to this work.

***Corresponding author:**
Saleem Ramadan
(saleem.ramadan@htu.edu.jo)

Citation: Ramadan S, Abu-Shams M. Optimizing 3D printing parameters for lightweight and high-strength unmanned aerial vehicle parts. *Mater Sci Add Manuf*. 2026;5(1):025290065.
doi: 10.36922/MSAM025290065

Received: July 18, 2025

Revised: August 4, 2025

Accepted: August 14, 2025

Published Online: October 8, 2025

1. Introduction

Unmanned aerial vehicles (UAVs) are important tools in the energy field due to their ability to access places that are inaccessible to humans. In renewable energy applications, UAVs are extensively used to monitor photovoltaic arrays and to assess weather conditions that can affect energy production and grid stability, among other applications. With the use of high-resolution cameras and thermal sensors, UAVs can

efficiently inspect photovoltaic arrays, detect faults, dirt buildup, and hotspots without the need for manual work, and shut down the system.[1] Moreover, UAVs can also be used as mobile weather stations to collect real-time data on temperature, humidity, and wind. This is important for improving energy forecasting and grid management.[2] For UAVs to perform well and have long flight times, they need to be designed with a high strength-to-weight ratio. Reducing the mass helps save battery and increases flight duration, allowing UAVs to cover larger areas and complete inspections more efficiently. Therefore, UAVs favor parts that are extremely lightweight but also strong enough to support flight efficiency and payload capacity.[3]

In recent years, additive manufacturing (AM) has played a significant and revolutionary role in applications across fields, including automotive, aerospace, medical, goods, food, and construction.[4-7] In complex and specialized industries, such as aviation, aerospace, and automotive, AM has been used to produce tools, parts, and components, as well as being involved in repair and restoration processes.[8-11] For example, fused deposition modeling (FDM) is a low-cost AM process, offering good flexibility for adjusting parameters such as layer height, raster orientation, and extrusion temperature, all of which directly affect the tensile strength of printed parts.[12,13] In addition, techniques such as design of experiments (DoE), including Taguchi method and response surface methodology (RSM), have been successfully used in literature to study the relationships between parameters and desired properties.[12,14,15] Moreover, multi-objective optimization methods, such as gray relational analysis and genetic algorithms, were used to compromise among tensile strength, elastic modulus, and strain at maximum stress for the printed parts.[16] Taguchi-based studies have shown that build orientation, raster angle, layer height, and extrusion temperature strongly affect the tensile properties of polylactic acid (PLA).[17,18] The mechanical properties of FDM-printed UAV parts are highly sensitive to process parameters.[19]

Recent achievements in composite filament materials, such as carbon fiber-reinforced PLA, enable the production of UAV parts with high strength-to-weight ratios and enhanced vibration stability.[1,20] AM techniques can increase the structural and aerodynamic efficiency of UAVs. With on-site/demand production capabilities, AM can effectively address supply chain issues and minimize operational costs.[21] For example, Huang *et al.*[22] developed a framework to design and produce topologically optimized, continuous carbon fiber-reinforced composites with both high manufacturing efficiency and manufacturability, and experimentally validated via material extrusion for a UAV wing spar that exceeded 1 m. They used 3D printing to produce the internal wing structure, while experimental tests and numerical analyses were conducted to validate the load-carrying capability. Similarly, Goh *et al.*[23] investigated the ability of the fused filament fabrication technique to fabricate geometrically hard-to-manufacture parts with continuous carbon fiber-reinforced thermoplastic. They found that the technique has a strong capability to print geometrically complex, high-performance structural parts for manufacturing a topology-optimized UAV landing gear.

To further enhance component performance, recent research has been using multi-objective optimization methods. For example, Grey–Taguchi techniques have been employed to optimize tensile strength, flexural strength, and shrinkage in PLA parts,[24,25] while genetic algorithms combined with RSM are effective in enhancing both mechanical strength and surface quality of FDM.[26] Meanwhile, advanced design methods, such as topology optimization and finite element analysis, have been used to create high-strength, lightweight UAV frames made from PLA and acrylonitrile butadiene styrene,[12,13] while composite filament materials can further enhance structural performance compared to traditional metals.[27]

Although progress has been made in understanding how FDM parameters affect PLA's mechanical properties, there is still a lack of integrated DoE frameworks that combine RSM with optimization, especially for the design of UAV parts. Limited studies focus on minimizing mass and maximizing tensile strength for UAV parts simultaneously. Therefore, this study filled this gap by using an RSM to systematically adjust FDM parameters, aiming to minimize mass while maximizing tensile strength of PLA parts for UAV applications. Then, the non-dominated sorting genetic algorithm II (NSGA-II) Pareto front analysis (using Python) and the Response Optimizer in Minitab were used to identify the optimal set of parameters to achieve the optimal strength-to-weight ratio.

2. Materials and methods

In this study, eight printing parameters were considered: Infill percentage, layer height, number of walls, nozzle temperature, printing speed, build plate temperature, number of bottom and upper layers, and infill pattern. When using the Taguchi L16 orthogonal design, four printing parameters were identified as the most influential factors: Infill percentage, layer height, number of walls, and build plate temperature. These four printing factors were selected and systematically varied using an RSM framework to study their influence on two response variables: Mass and tensile strength. RSM was chosen because it is a robust

statistical method for modeling and optimizing complex processes affected by multiple variables. It allows for the exploration of how process parameters affect responses, considering both linear and interactional effects, making it well-suited for processes such as FDM, where several parameters interact simultaneously.

The experimental results were then used to develop two regression models, one for mass and the other for tensile strength of a specimen. These models show how the four parameters affect their corresponding response variable. To identify the optimal combination of printing parameters that can both maximize the tensile strength and minimize the mass of the printed parts, two optimization methods were used simultaneously: NSGA-II Pareto front analysis (performed in Python) and the Response Optimizer tool in Minitab.

The test specimens were first designed using SolidWorks 3D CAD (SolidWorks®, United States [US]), adopting the geometry, as shown in Figure 1A, and then exported in STL format to be processed in ideaMaker® software (version 2023, US). To ensure the specimen had good adhesion to the build plate, the first layer of each print was made with a 0.3-mm layer height and with a brim. All printing was conducted at room temperature, and each print was started only after both the nozzle and the build plate reached a temperature of 25°C.

The fabrication process was carried out on the E2 3D printer (Raise3D, China; Figure 1B) equipped with a 0.4-mm nozzle, using 1.75-mm PLA filament (tensile strength: 46.6 MPa, modulus of elasticity: 2,636 MPa, elongation: 1.9%). The mass of each printed specimen was measured using the FX-200i digital scale (capacity: 220 g; readability: 0.001 g; A&D Company, Limited, Japan; Figure 1C), allowing precise detection of small differences between test samples. The tensile strength was tested using the FS300CT universal testing machine (Testometric, United Kingdom; Figure 1D), equipped with a 2,500 kg load cell.

The NSGA-II, a popular evolutionary algorithm for multi-objective optimization, was used in this study to generate a Pareto front. Instead of yielding a single optimal solution, NSGA-II generates a group of solutions in which improving one goal (e.g., mass) usually entails a trade-off in another (e.g., tensile strength). As there is an inherent conflict between reducing mass and increasing strength—lighter UAV parts often lose structural strength, whereas stronger parts tend to weigh more and thus reduce flight time—NSGA-II is an excellent method to study these trade-offs. In this research, NSGA-II was applied to analyze the combined effects of infill percentage, layer height, number of walls, and build plate temperature on the mass and tensile strength of UAV frame parts. Using regression models derived from the RSM data, the algorithm tested hundreds of parameter combinations and generated a Pareto front that shows the optimal trade-offs between the two goals. This approach enables data-driven optimization of 3D-printed UAV parts, enhancing both flight efficiency and mechanical durability.

In addition, the Response Optimizer tool in Minitab was used to identify the optimal combination of input settings based on the response surface models derived

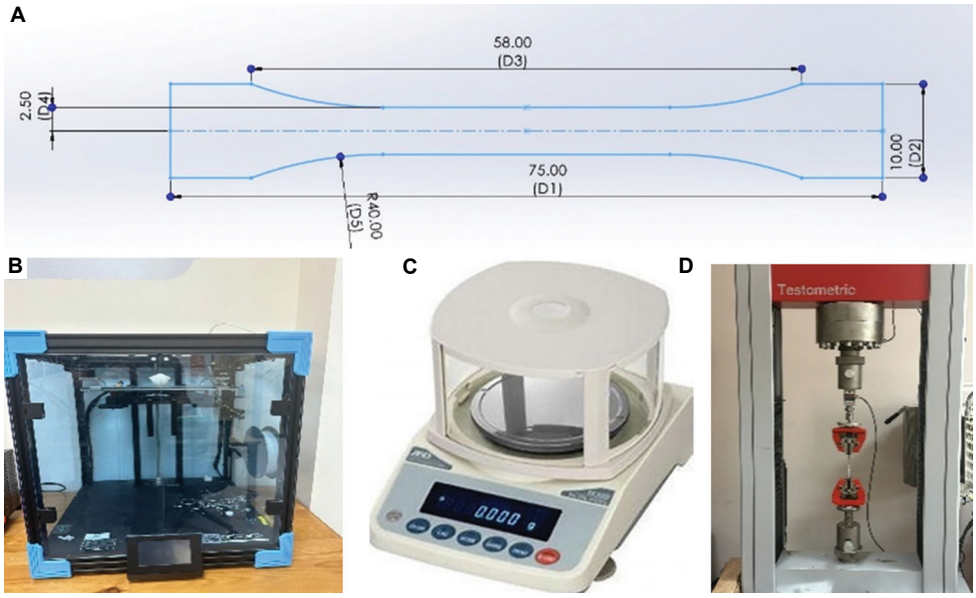

Figure 1. Specimen design and equipment used in the study. (A) Design of the test specimen (units in mm). (B) Fused deposition modeling 3D printer. (C) Digital weighing scale. (D) FS300CT testing machine

from RSM. It visualizes how input factors affect predicted outcomes and allows users to set goals (e.g., maximize tensile strength and minimize mass) and explore different combinations of input factors interactively. In this study, after modeling tensile strength and mass as functions of layer height, number of walls, infill percentage, and build plate temperature, the Response Optimizer was used to refine the selection of parameters—identifying combinations that achieve a balanced trade-off between high tensile strength and low mass for 3D-printed UAV parts.

This study presented an integrated method that combines RSM, NSGA-II Pareto front optimization, and Minitab's Response Optimizer to optimize FDM printing parameters for UAV parts. By modeling the effects of infill percentage, layer height, number of walls, and build plate temperature on both mass and tensile strength, and using multi-objective optimization, this research enables data-driven selection of printing parameters that balance lightweight design with mechanical performance. The resulting Pareto front and optimized parameter sets provide practical guidance for producing high-performance, lightweight UAV parts, enhancing flight endurance, energy efficiency, and structural strength in future drone designs. The flowchart of this study is shown in Figure 2.

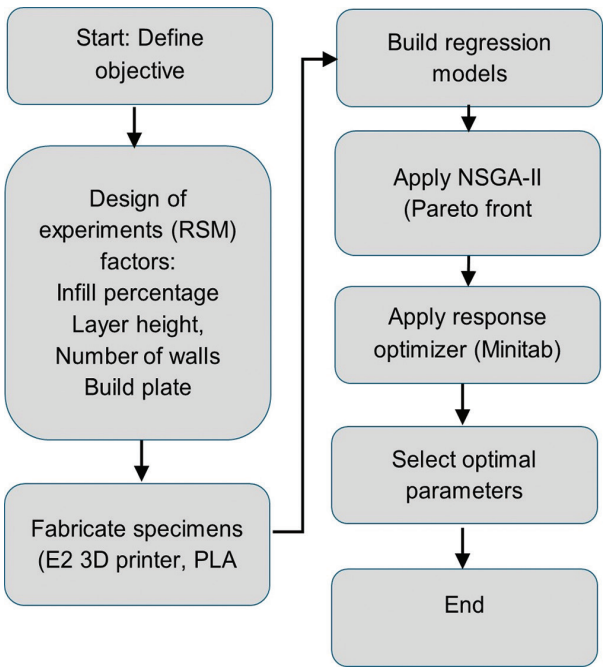

Figure 2. Methodology flowchart
Abbreviations: NSGA-II: Non-dominated sorting genetic algorithm II; PLA: Polylactic acid; RSM: Response surface methodology

3. Results

3.1. Analysis

In this study, RSM was employed to study the effects of four important FDM parameters on two response variables: Mass (g) and tensile strength (MPa). The selected parameters and their levels were: Infill percentage (40, 60, and 80%), which controls internal density; layer height (0.150, 0.175, and 0.250 mm), which affects bonding and surface finish; number of walls (2, 3, and 4), which impacts outer shell strength; and build plate temperature (45, 55, and 65°C), which influences adhesion and bonding between layers, such that if the temperature is too low, the material may shrink or warp, resulting in weak layer bonding (Table 1). These parameter ranges were selected to reflect practical process variations and to support the optimization of UAV parts for both high strength and low weight.

Table 2 presents the estimated regression coefficients for the mass of the designed UAV part. The analysis was conducted using uncoded units. RSM was employed instead of a full factorial design because the goals were not only to study the main effects and interactions between the factors but also to capture curvature in the responses (The design matrix for the RSM is provided in Supplementary Table S1). The squared terms—such as layer height × layer height—in Tables 2 and 3 indicate that the experiment was designed to model nonlinear relationships, which full factorial designs alone cannot model effectively without multiple levels. RSM allows for a more efficient exploration of the design space with fewer runs than a full factorial design, particularly when estimating second-order (quadratic) effects is important for optimization.

The model achieved a standard error of 0.01453, indicating a minimal difference between the observed values and the predicted regression line. The coefficient of determination (R^2) was 98.2%, and the adjusted R^2 was 98.0%. The high R^2, together with the minimal difference between R^2 and adjusted R^2, implies that the model explains nearly all of the variation in the response without evidence of overfitting. These results suggest that the predictors included in the model are important and that the model has strong and reliable predictive capability.

Table 1. Parameter ranges

Parameter	Min	Max
Infill percentage (%)	40	80
Layer height (mm)	0.15	0.25
Number of walls	2	4
Build plate temperature (°C)	45	65

Table 2. Regression coefficients for mass

Term	Coefficient	SE	*t*	*p*-value
Constant	0.67991	0.108492	6.267	<0.001*
Infill percentage	0.00999	0.001329	7.522	<0.001*
Layer height	0.65440	0.293337	2.231	0.027*
Number of perimeters	0.20984	0.026571	7.897	<0.001*
Build plate temperature	−0.00245	0.004509	−0.543	0.588
Infill percentage × infill percentage	−0.00000	0.000010	−0.270	0.788
Layer height × layer height	7.62339	0.717095	10.631	<0.001*
Number of walls × number of walls	−0.00815	0.004034	−2.020	0.045*
Build plate temperature × build plate temperature	0.00004	0.000040	0.890	0.375
Infill percentage × layer height	−0.01770	0.001083	−16.339	<0.001*
Infill percentage × number of walls	−0.00082	0.000081	−10.086	<0.001*
Infill percentage × build plate temperature	−0.00001	0.000008	−1.176	0.242
Layer height × number of walls	−0.28399	0.021660	−13.111	<0.001*
Layer height × build plate temperature	−0.00441	0.002166	−2.037	0.044*
Number of perimeters × build plate temperature	−0.00014	0.000162	−0.870	0.386

Notes: Significance level is set at p=0.05, *indicates p<0.05.

Table 3. Regression coefficients for tensile strength

Term	Coefficient	SE	t	*p*-value
Constant	−0.830	10.3567	−0.080	0.936
Infill percentage	0.357	0.1268	2.815	0.006*
Layer height	104.608	28.0020	3.736	0.000*
Number of walls	11.915	2.5365	4.698	0.000*
Build plate temperature	−0.185	0.4304	−0.429	0.669
Infill percentage × infill percentage	−0.002	0.0010	−1.561	0.121
Layer height × layer height	20.605	68.4540	0.301	0.764
Number of walls × number of walls	−0.902	0.3851	−2.343	0.021*
Build plate temperature × build plate temperature	0.003	0.0039	0.764	0.446
Infill percentage × layer height	−0.602	0.1034	−5.825	0.000*
Infill percentage × number of walls	−0.007	0.0078	−0.896	0.372
Infill percentage × build plate temperature	0.001	0.0008	0.699	0.485
Layer height × number of walls	−8.912	2.0677	−4.310	0.000*
Layer height × build plate temperature	−0.299	0.2068	−1.446	0.150
Number of walls × build plate temperature	−0.018	0.0155	−1.192	0.235

Notes: Significance level is set at p=0.05, *indicates p<0.05.

Figure 3 presents the normal probability plot for mass, where most residuals lie close to the reference line, with only minor deviations at the tails, indicating that the assumption of normally distributed residuals is largely met. Figure 4 shows the histogram of residuals, which is nearly symmetric and bell-shaped, centered around zero. Together, these plots suggest that the regression model for mass fits the data well, with no serious violations of the normality assumption, thereby confirming the reliability of the statistical results.

The regression results presented in Table 2 show that infill percentage, layer height, and number of walls have significant positive effects on mass (p<0.05), meaning that increasing any of these parameters raises mass. In contrast, build plate temperature showed no significant effect (p=0.588). Several interaction terms were highly significant, especially infill percentage × layer height, infill percentage × number of walls, and layer height × number of walls (all p<0.001), suggesting that combinations of these parameters strongly influence mass. The significant squared terms for layer height and number of walls also indicate that their relationships with mass are nonlinear, where the effect of increasing these parameters is not

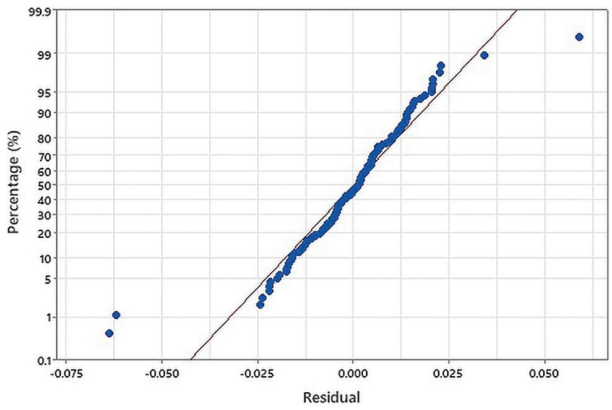

Figure 3. Normal probability plot for mass

constant across all levels. Meanwhile, terms involving the build plate temperature were mostly not significant. Overall, the findings suggest that controlling the mass of printed parts mainly depends on adjusting infill percentage, layer height, and number of walls, along with their interactions, while build plate temperature has minimal impact. This result is also illustrated in the Pareto chart of standardized effects for mass (Figure 5), using a reference line of 1.98.

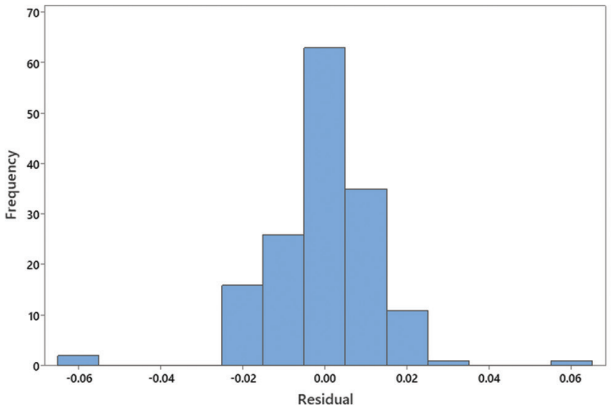

Figure 4. Histogram of residuals for mass

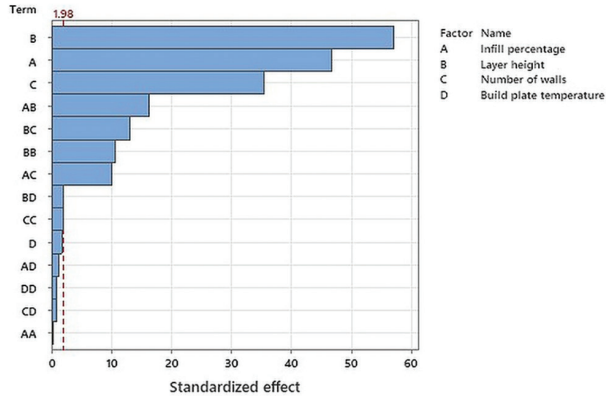

Figure 5. Pareto chart of standardized effects for mass

Figure 6A shows the main effects of the selected parameters on the average mass of the printed parts, indicating that infill percentage, layer height, and number of walls each have a strong positive effect on mass—when these parameters increase, the mass of the part also increases. In contrast, the build plate temperature has minimal effect. Figure 6B presents the interaction effects, confirming that mass increases even further when a higher layer height is combined with a higher number of walls. The interactions between infill percentage and either layer height or number of walls also show a clear increasing trend. In general, these results demonstrate that infill percentage, layer height, and number of walls are the primary factors influencing mass, both individually and in combination, whereas build plate temperature has minimal influence.

Figure 7 shows the contour plots for mass, illustrating the interaction effects of the selected parameters on the mass of the printed parts. Each plot presents how pairs of parameters—layer height, infill percentage, number of walls, and build plate temperature—interact to affect mass, with the other factors held constant. The results show that increasing layer height and number of walls leads to a clear increase in mass, while infill percentage has a smaller but noticeable effect. Build plate temperature, in contrast, has minimal impact on mass across its range. These findings suggest that careful adjustment of layer height and number of walls is important when aiming to reduce the mass of UAV parts.

Figure 8 presents the surface plots for mass, illustrating how the selected parameters jointly affect the mass of the printed parts. The surfaces demonstrate that increasing layer height and number of walls leads to substantial increases in mass, with a pronounced nonlinear trend—particularly for the number of walls. Infill percentage also increases the mass, but the effect is more gradual and mostly linear. Build plate temperature, in contrast, shows minimal influence, as indicated by the nearly flat surfaces in its plots. Overall, these results confirm that layer height and number of walls are the most important parameters to control when aiming to reduce the mass of UAV parts, and they must be adjusted carefully to achieve lightweight designs.

The regression equation (Equation I) for mass supports the trends observed in the main effects and interaction plots. The positive coefficients for infill percentage, layer height, and number of walls indicate that increasing any of these parameters increases the mass of the part, consistent with the strong upward trends in the main effects plots. The coefficient for the build plate temperature was close to zero, consistent with its minimal influence shown in earlier results. The significant squared terms for layer height and number of walls also reflect the curvature seen in their plots. The negative interaction terms (such as infill percentage × layer height and layer height × number of walls) suggest that when both these parameters are set to higher levels, the increase in mass is smaller than would be expected from simply adding their individual effects—this pattern is also visible in the interaction plots. In general, the regression equation provides a clear mathematical summary of the findings: layer height, number of walls, and infill percentage are the primary factors affecting mass, while build plate temperature has little effect.

$$\text{Mass} = 0.679909 + 0.00999339 \times IP + 0.654401 \times LH + 0.209838 \times NW - 0.00244999 \times BT - 2.72106E - 6 \times IP^2 + 7.62339 \times LH^2 - 0.00814842 \times NW^2 + 3.59158E - 5 \times BT^2 - 0.0176952 \times IP \times LH - 8.19231E - 4 \times IP \times NW - 9.54812E - 6 \times IP \times BT - 0.283995 \times LH \times NW - 0.00441283 \times LH \times BT - 1.41288E - 4 \times NW \times BT \quad \text{(I)}$$

where:

- IP = Infill percentage
- LH = Layer height (mm)
- NW = Number of walls
- BT = Build plate temperature (°C).

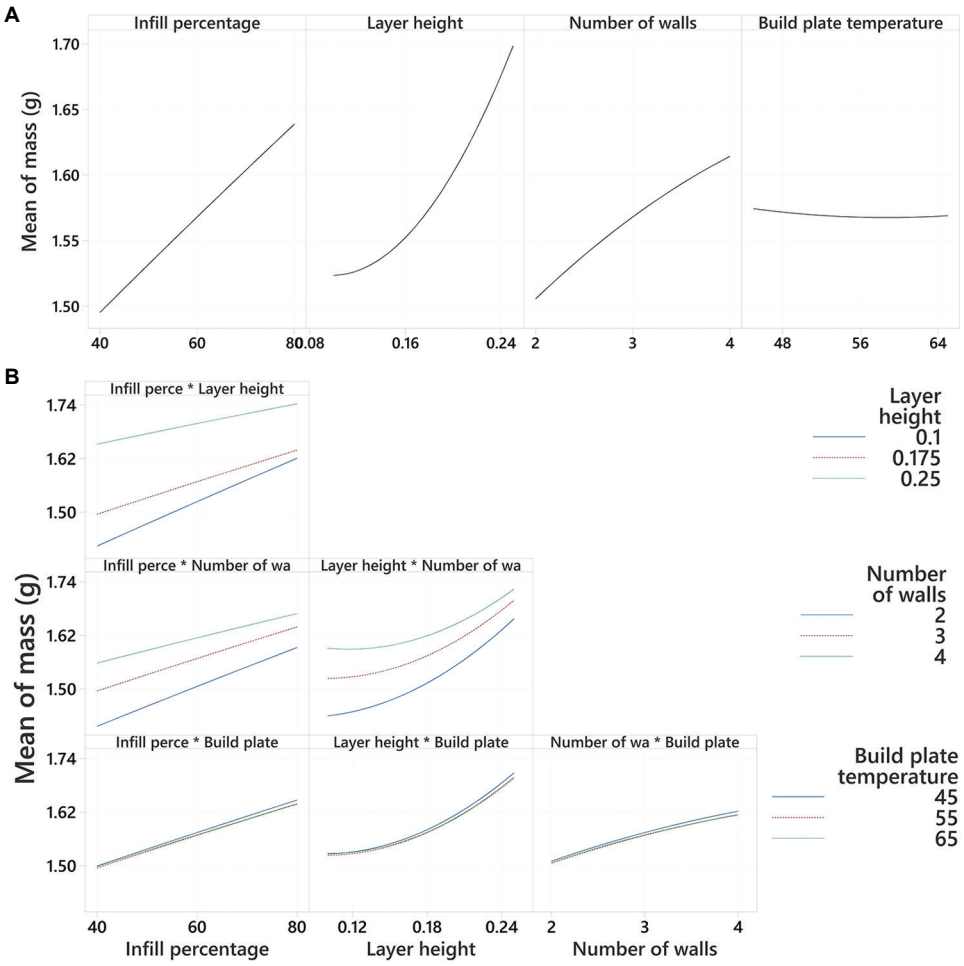

Figure 6. Factorial plots for mass. (A) Plots for individual parameters. (B) Plots for interaction effects

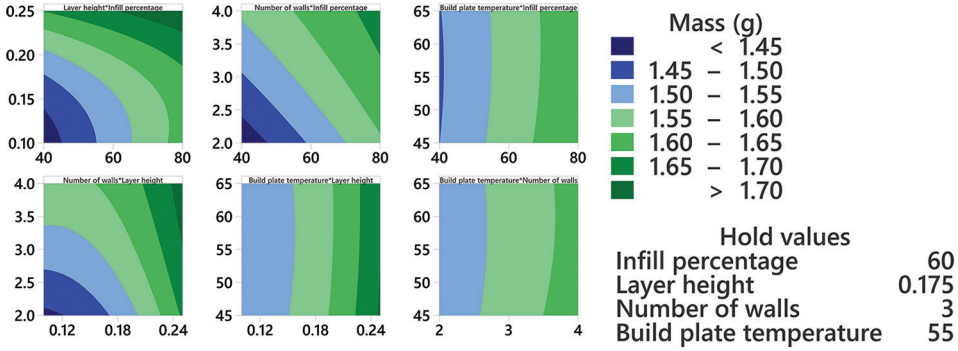

Figure 7. Contour plots for mass
Notes: Darker blue areas represent lower mass; Darker green areas represent higher mass

Table 3 presents the estimated regression coefficients for the tensile strength of the designed UAV part. The analysis was performed using uncoded units. The model produced a standard error of 1.387, indicating a minimal difference between the observed values and the predicted regression line. The R^2 showed that 88.5% of the variation

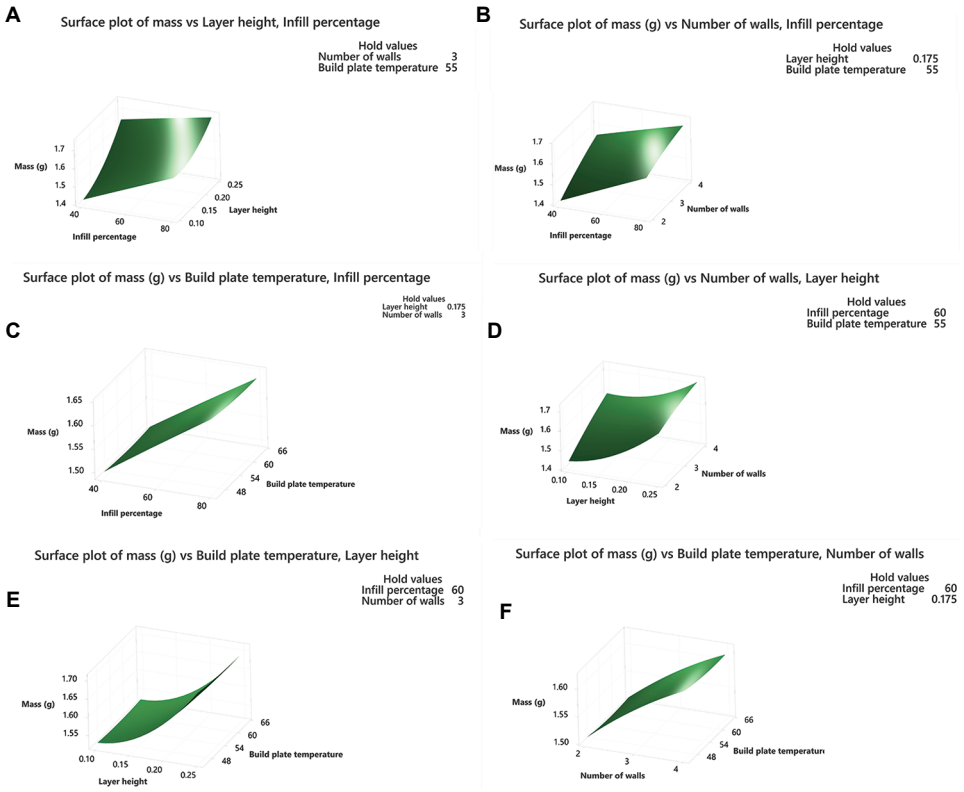

Figure 8. Surface plots for mass. (A) Mass versus LH versus IP. (B) Mass versus NW versus IP. (C) Mass versus BT versus IP. (D) Mass versus BT versus LH. (E) Mass versus NW versus LH. (F) Mass versus BT versus NW
Abbreviations: BT: Build plate temperature; IP: Infill percentage; LH: Layer height; NW: Number of walls.

in the response variable is explained by the model, while the adjusted R^2 of 87.3% was closely aligned, suggesting a good balance between explanatory power and simplicity without evidence of overfitting. The normal probability plot of residuals (Figure 9) shows that the residuals closely follow the reference line, indicating they are approximately normally distributed. The histogram of residuals (Figure 10) displays a roughly bell-shaped curve centered near zero, further supporting normality. Together, these results suggest that the assumptions of normality and homoscedasticity are reasonably met, reinforcing the reliability of the regression model for tensile strength.

The regression analysis results (Table 3) show that infill percentage, layer height, and number of walls have significant effects on tensile strength (p<0.05), whereas build plate temperature has no significant effect (p=0.669). Among the interaction terms, infill percentage × layer height and layer height × number of walls showed strong negative effects with high significance (p<0.001), meaning that combinations of these parameters strongly influence tensile strength. In addition, the term number of walls × number of walls was also significant (p=0.021), while other

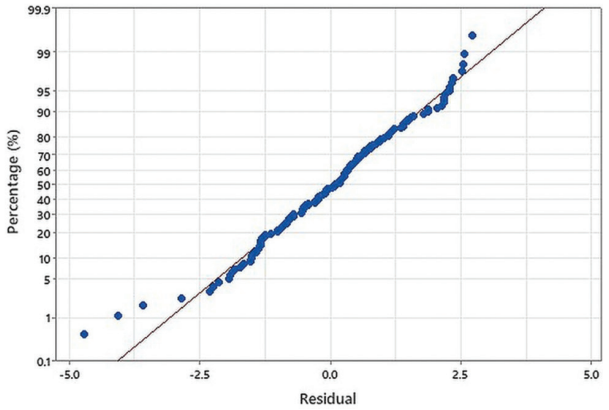

Figure 9. Normal probability plot for tensile strength

higher-order terms showed weaker or non-significant effects. Overall, the findings suggest that tensile strength is primarily affected by layer height, number of walls, infill percentage, and certain key interactions between these parameters. This result is also illustrated in the Pareto chart of standardized effects for tensile strength (Figure 11), using a reference line of 1.98.

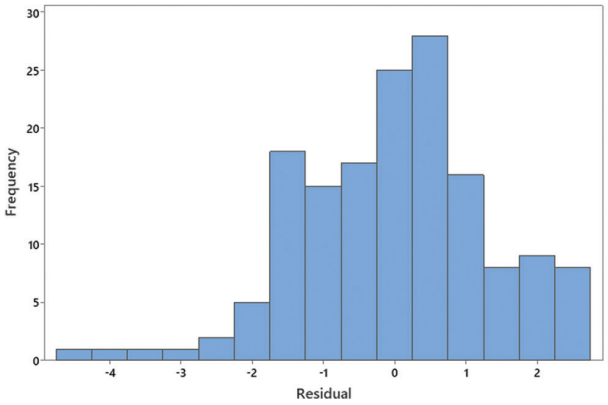

Figure 10. Histogram for tensile strength

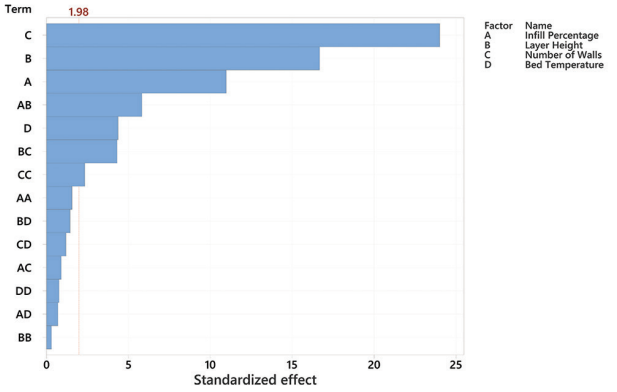

Figure 11. Pareto chart of standardized effects for tensile strength
Abbreviations: BT: Build plate temperature; IP: Infill percentage; LH: Layer height; NW: Number of walls

Figure 12A shows the main effects plots for tensile strength, indicating that increasing infill percentage, layer height, and number of walls all lead to higher tensile strength, whereas build plate temperature has only a smaller positive effect. Figure 12B presents the interaction effects between the primary parameters. Notably, there were strong interactions between infill percentage and layer height, as well as between layer height and number of walls, where higher combinations of these parameters result in greater tensile strength. The interactions between other factors were comparatively weak. In general, these results indicate that optimizing tensile strength requires careful adjustment of both the primary effects and the key interactions among the primary parameters.

The contour plots (Figure 13) show the interaction effects of the key parameters on tensile strength. Across the combinations of layer height, infill percentage, number of walls, and build plate temperature, higher tensile strength occurs when both layer height and number of walls are increased, as well as when infill percentage is higher. The plots also highlight the importance of interactions—particularly between layer height and infill percentage, and between number of walls and layer height—in achieving higher tensile strength. These visual trends reinforce that optimizing combinations of parameters, rather than adjusting individual factors in isolation, is necessary for producing high-performance printed parts.

Figure 14 presents the 3D surface plots, demonstrating the combined effects of the key FDM process parameters on tensile strength. The surfaces indicate that increasing layer height, infill percentage, and number of walls generally results in higher tensile strength. The curvature in the surfaces demonstrates that these relationships are not purely linear, confirming the presence of significant interaction and quadratic effects. This curvature reflects the complex interplay between parameters and underscores the need for multi-parameter optimization strategies to achieve superior mechanical performance in 3D-printed parts. The squared and interaction terms in the regression model account for this nonlinear behavior, explaining why the surfaces bend rather than remain flat, highlighting that optimal performance requires coordinated adjustment of parameters rather than isolated changes.

While the tensile strength tests were carried out on specific, individual samples, the smooth curves, as shown in Figure 14, were generated from the regression model developed through RSM. This model uses the experimental data to predict values across the entire range of input settings, effectively "connecting the dots" between the tested points. As a result, it is possible to visualize a continuous surface, even though the actual tests were conducted at discrete parameter combinations. The model fills in these gaps, providing a clearer picture of how the parameters interact across the design space.

The regression equation (Equation II) for tensile strength indicates that layer height and number of walls have the largest positive linear effects, with layer height contributing the most, consistent with the trends observed in the main-effects plot. Infill percentage also has a positive effect on strength, but with a smaller impact. The small negative linear effect of build plate temperature suggests a limited influence, aligning with the patterns shown in the main effects and interaction plots. The negative quadratic terms for infill percentage (IP^2) and number of walls (NW^2) indicate diminishing returns at higher values, while the positive quadratic term for layer height (LH^2) suggests a strong nonlinear increase in strength as layer height rises. The significant interaction terms, particularly

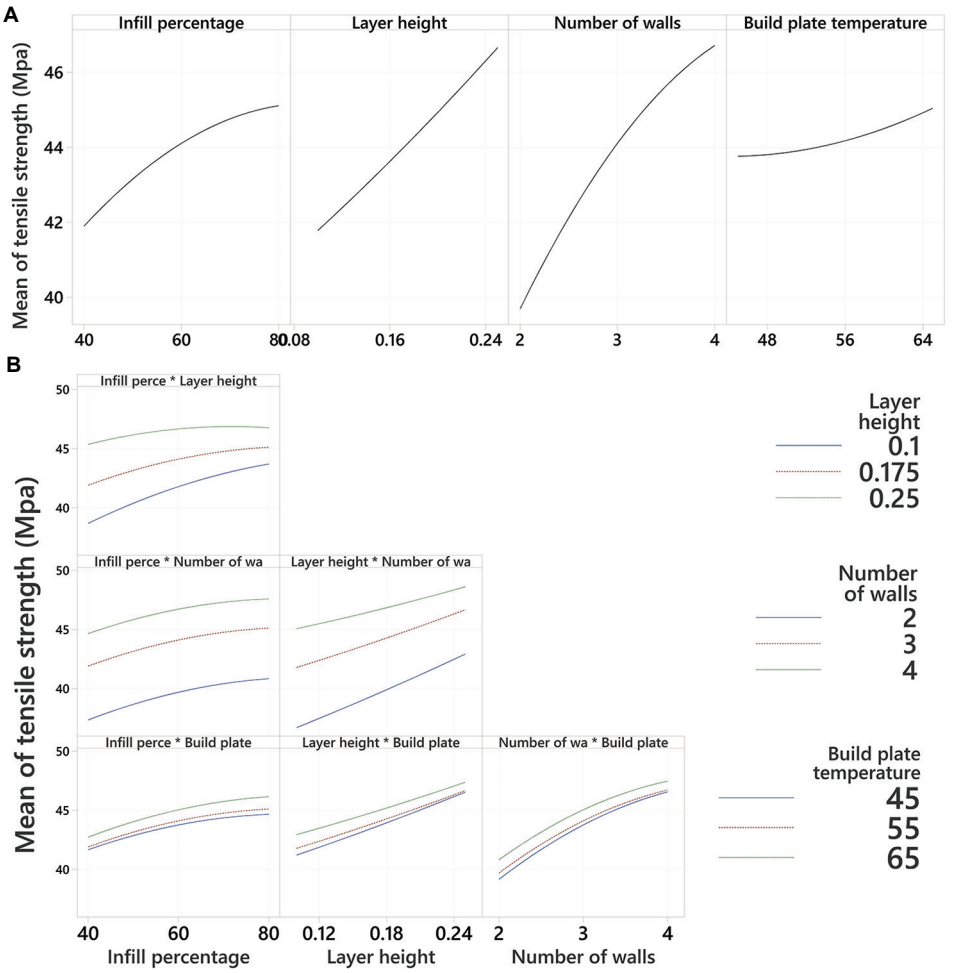

Figure 12. Factorial plots for tensile strength. (A) Plots for individual parameters. (B) Plots for interaction effects
Abbreviations: BT: Build plate temperature; IP: Infill percentage; LH: Layer height; NW: Number of walls

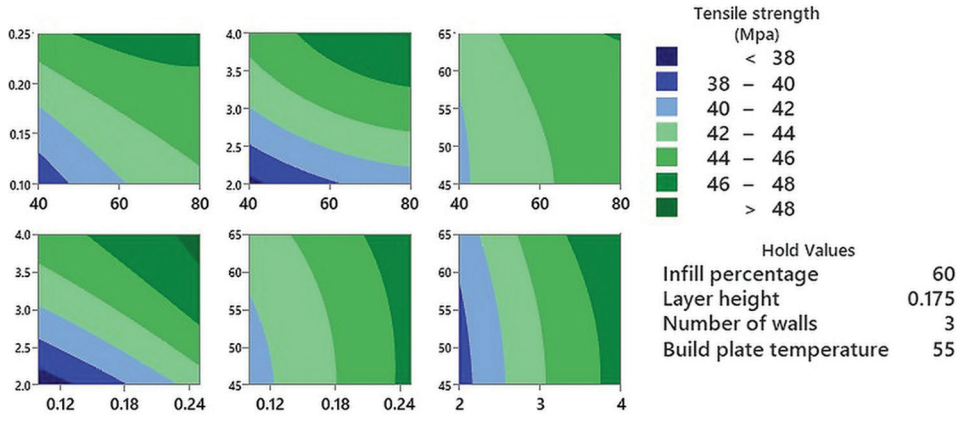

Figure 13. Contour plots for tensile strength
Notes: Darker blue areas represent lower mass; Darker green areas represent higher mass

layer height × number of walls and infill percentage × layer height, highlight the importance of combined parameter effects in achieving optimal tensile strength, as further confirmed by the interaction and contour plots. Overall,

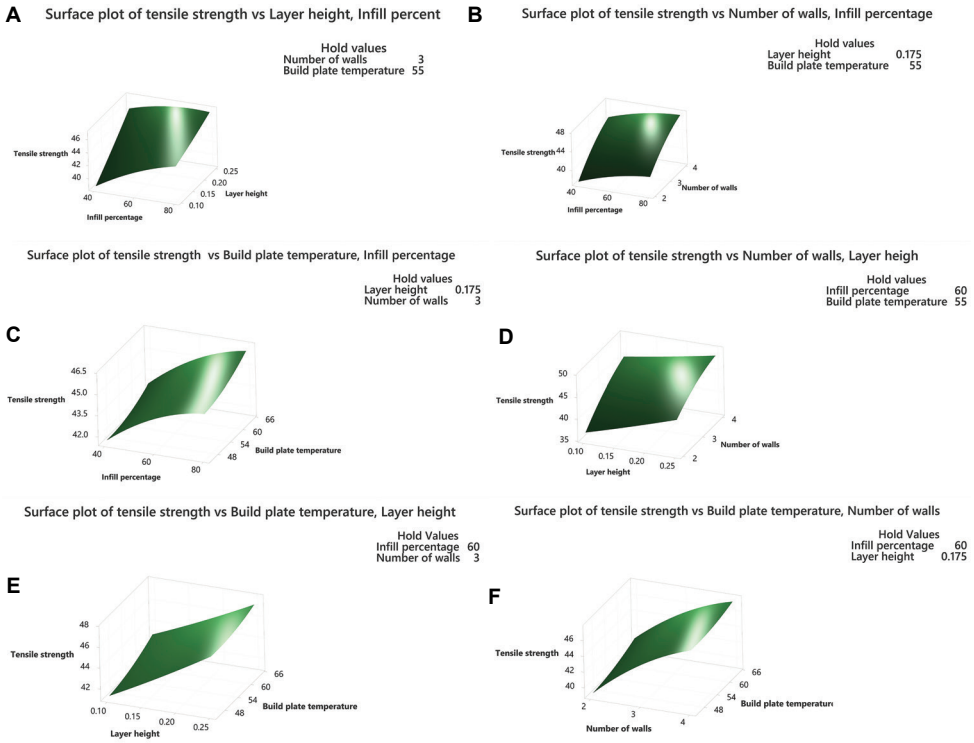

Figure 14. Surface plots for tensile strength. (A) Tensile strength versus LH versus IP. (B) Tensile strength versus NW versus LH. (C) Tensile strength versus NW versus IP. (D) Tensile strength versus BT versus LH. (E) Tensile strength versus BT versus IP. (F) Tensile strength versus BT versus NW
Abbreviations: BT: Build plate temperature; IP: Infill percentage; LH: Layer height; NW: Number of walls

the model identifies layer height, number of walls, and their interactions as the most important factors in optimizing tensile strength for the printed parts.

$$\text{Tensile strength} = -0.830244 + 0.356997 \times IP + 104.608 \times LH + 11.9154 \times NW - 0.184526 \times BT - 0.00150299 \times IP^2 + 20.6051 \times LH^2 - 0.901996 \times NW^2 + 0.00294304 \times BT^2 - 0.602183 \times IP \times LH - 0.00695 \times IP \times NW + 0.000542375 \times IP \times BT - 8.912 \times LH \times NW - 0.299033 \times LH \times BT - 0.01849 \times NW \times BT \quad \text{(II)}$$

Where:

- *IP* = Infill percentage
- *LH* = Layer height (mm)
- *NW* = Number of walls
- *BT* = Build plate temperature (°C).

After building the regression models for mass and tensile strength, these models were used to generate a Pareto front (Figure 15) to illustrate the trade-off between the two objectives: As tensile strength increases, mass also tends to increase. Each point on the curve represents an optimal combination of process parameters, where improving one objective (e.g., increasing strength) compromises the other (e.g., higher mass). The curve shows a smooth trade-off, with diminishing returns at the higher end of tensile strength, meaning that further gains in strength require disproportionately large increases in mass. When designing UAV parts, it is crucial to strike a balance between low weight and sufficient strength. Overemphasis on one aspect often comes at the cost of the other. Based on experience with FDM optimization in aerospace settings, the most reliable outcomes are typically achieved with parameter settings positioned in the mid-range rather than at the extremes. In this case, aiming for a tensile strength of 46 to 48 MPa and a mass of 1.5 to 1.6 g has proven to be an effective middle ground, delivering structural performance while supporting longer flight durations.

The response optimizer plot from Minitab (Figure 16) provides a visual summary of how each process parameter affects the two target responses—tensile strength (to be maximized) and mass (to be minimized). The optimizer identified the optimal combination of parameters as: Infill percentage of 58.26%, layer height of 0.1635 mm, number of walls of 4, and build plate temperature of 65°C. Under these settings, the model predicted a tensile strength of 47.08 MPa and an actual mass of 1.60 g, with a high composite desirability score of 0.9149. The individual desirability values indicate that mass was minimized almost perfectly (0.99944), while tensile strength reached a high value (0.83756), slightly below the target of 50

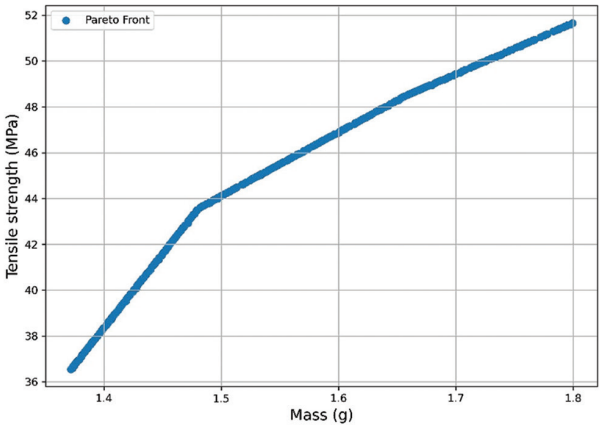

Figure 15. Pareto front analysis of mass versus tensile strength

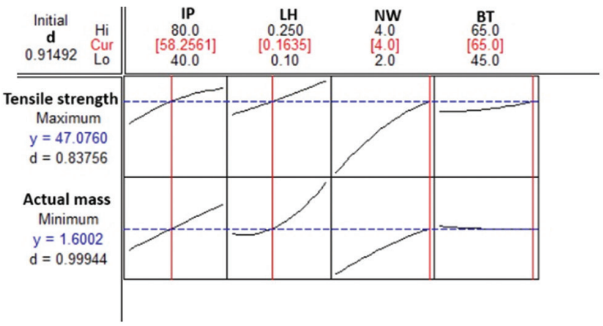

Figure 16. Response optimizer plot
Abbreviations: BT: Build plate temperature; IP: Infill percentage; LH: Layer height; NW: Number of walls

MPa. In the optimizer plot, the curves for each parameter illustrate the sensitivity of the responses to changes in the parameters:

- An increase in the number of walls and layer height substantially enhances tensile strength (as also seen in the Pareto front and interaction plots), but also increases mass.
- Infill percentage has a positive but smaller effect on strength and increases mass.
- Build plate temperature has a smaller but still positive influence on tensile strength at higher values.

The red vertical lines in the plot indicate the parameter settings selected by the optimizer, representing a balance between the two responses rather than maximizing one at the cost of the other. The balance was reflected in the high composite desirability of 0.91, very close to 1, meaning that both objectives were well satisfied simultaneously. Compared with the Pareto front results, this solution was located near the "knee" of the curve, the ideal area where further gains in tensile strength would require a disproportionately large increase in mass, thereby reducing flight efficiency. As such, the optimized configuration achieved an excellent balance between strength and weight, making it highly suitable for UAV applications where both mechanical performance and lightweight design are critical.

3.2. Validation

To verify the selected parameters, five specimens were produced using these exact settings. Their tensile strength and mass were then measured and compared with the values predicted by Equations I and II. The results are summarized in Table 4. The tensile strength showed a percentage error of less than 4.5%, while the error for mass was below 2.5%. These findings demonstrate that tensile strength and mass are highly affected by infill percentage, layer height, number of walls, and build plate temperature. With accurate control of these parameters, the tensile strength and mass of 3D-printed UAV parts can be reliably predicted.

4. Discussion

This work developed and validated an integrated optimization framework for producing lightweight and high-strength UAV parts through FDM. Through a detailed analysis of the effects of infill percentage, layer height, number of walls, and build plate temperature on both mass and tensile strength, and by applying RSM, NSGA-II Pareto optimization, and Minitab's Response Optimizer, the study offers valuable guidance for optimizing FDM parameters for UAV applications.

The regression models demonstrated strong predictive accuracy for both response variables (R^2 = 98.2% for mass; R^2 = 88.5% for tensile strength), confirming that infill percentage, layer height, and number of walls are the most significant factors, whereas build plate temperature has minimal direct influence. The findings also revealed clear trade-offs: Increasing layer height and number of walls enhances tensile strength but also increases mass. By carefully adjusting infill percentage, it is possible to balance both targets effectively.

The Pareto front analysis provided a clear visualization of this trade-off and identified a "knee" region where further increases in strength would come at the cost of greater mass. The Response Optimizer tool recommended an optimal parameter set: Infill percentage of 58.26%, layer height of 0.1635 mm, number of walls of 4, and build plate temperature of 65°C. Using these settings, the model predicted a tensile strength of 47.08 MPa and mass of 1.60 g, with a composite desirability of 0.9149. The validation phase, which involved fabricating test specimens with the optimal parameters, confirmed the effectiveness of this method. The percentage error for tensile strength

Table 4. Predicted versus actual tensile strength (TS) and mass

No.	Actual TS (Mpa)	Predicted TS (Mpa)	Predicted error (%)	Actual mass (g)	Predicted mass (g)	Predicted error (%)
1	47.803	47.080	−1.54	1.594	1.606	−0.93
2	45.0113		4.39	1.583		1.43
3	45.083		4.24	1.605		0.06
4	48.656		−3.35	1.642		−2.24
5	45.018		4.38	1.591		0.93

TS: Tensile strength

was below 4.5%, and for mass below 2.5%, demonstrating that infill percentage, layer height, number of walls, and build plate temperature strongly influence both properties in FDM-based printed parts. This optimized configuration offers a practical balance for UAV applications, where flight efficiency and structural strength are equally important.

5. Conclusion

In summary, this study presents a reliable, data-driven approach for optimizing FDM-based printed UAV parts. The same methodology can be extended to other lightweight structural or aerial applications where strength and low mass are key requirements. Future work can explore the use of advanced materials (such as carbon fiber-reinforced filaments), test larger UAV designs, and further refine the optimization models through validation under actual flight conditions.

Acknowledgments

None.

Funding

None.

Conflict of interest

The authors declare they have no competing interests.

Author contributions

Conceptualization: Saleem Ramadan
Formal analysis: Saleem Ramadan, Mohammad Abu-Shams
Investigation: Saleem Ramadan, Mohammad Abu-Shams
Methodology: Mohammad Abu-Shams, Saleem Ramadan
Writing–original draft: Saleem Ramadan, Mohammad Abu-Shams
Writing–review & editing: Mohammad Abu-Shams, Saleem Ramadan

Ethics approval and consent to participate

Not applicable.

Consent for publication

Not applicable.

Availability of data

The data supporting the findings of this study are available from the corresponding author upon reasonable request.

References

1. Barua A, Singha S. *Simulation Studies for Structural Optimization of A 3D Printable Quadcopter*. *Conference: 6th International Conference on Mechanical Industrial and Materials Engineering*; 2024.
2. Chodorek A, Chodorek R, Yastrebov A. Weather sensing in an urban environment with the use of a UAV and WebRTC-based platform: A pilot study. *Sensors (Basel)*. 2021;21:7113.
   doi: 10.3390/s21217113
3. Laghari AA, Jumani AK, Laghari RA, Nawaz H. Unmanned aerial vehicles: A review. *Cogn Robotics*. 2023;3:8-22.
   doi: 10.1016/J.COGR.2022.12.004
4. Praveena BA, Lokesh N, Buradi A, Santhosh N, Praveena BL, Vignesh R. A comprehensive review of emerging additive manufacturing (3D printing technology): Methods, materials, applications, challenges, trends and future potential. *Mater Today Proc*. 2022;52:1309-1313.
   doi: 10.1016/J.MATPR.2021.11.059
5. Shoeb M, Kumar L, Haleem A, Javaid M. Trends in additive manufacturing: An exploratory study. In: *Advances in Additive Manufacturing: Artificial Intelligence, Nature-Inspired, and Biomanufacturing*. Netherlands: Elsevier; 2023. p. 15-25.
   doi: 10.1016/B978-0-323-91834-3.00027-2
6. Klenam DEP, McBagonluri F, Asumadu TK, *et al.* Additive manufacturing: Shaping the future of the manufacturing industry - overview of trends, challenges and opportunities. *Appl Eng Sci*. 2025;22:100224.
   doi: 10.1016/J.APPLES.2025.100224
7. Kanishka K, Acherjee B. Revolutionizing manufacturing: A comprehensive overview of additive manufacturing processes, materials, developments, and challenges. *J Manuf Process*. 2023;107:574-619.

doi: 10.1016/J.JMAPRO.2023.10.024

8. Blakey-Milner B, Gradl P, Snedden G, *et al.* Metal additive manufacturing in aerospace: A review. *Mater Des*. 2021;209:110008.

   doi: 10.1016/J.MATDES.2021.110008

9. Khan N, Riccio A. A systematic review of design for additive manufacturing of aerospace lattice structures: Current trends and future directions. *Prog Aerospace Sci*. 2024;149:101021.

   doi: 10.1016/J.PAEROSCI.2024.101021

10. Alami AH, Ghani Olabi A, Alashkar A, *et al.* Additive manufacturing in the aerospace and automotive industries: Recent trends and role in achieving sustainable development goals. *Ain Shams Eng J*. 2023;14(11):102516.

    doi: 10.1016/J.ASEJ.2023.102516

11. Espadinha-Cruz P, Reboredo E. A fuzzy system to measure additive manufacturing maturity: A case study in the automotive industry. *Procedia Comput Sci*. 2025;253:1402-1411.

    doi: 10.1016/J.PROCS.2025.01.202

12. Zaman UK, Boesch E, Siadat A, Rivette M, Baqai AA. Impact of fused deposition modeling (FDM) process parameters on strength of built parts using Taguchi's design of experiments. *Int J Adv Manuf Technol*. 2019;101(5):1215-1226.

    doi: 10.1007/s00170-018-3014-6

13. Heidari-Rarani M, Ezati N, Sadeghi P, Badrossamay MR. Optimization of FDM process parameters for tensile properties of polylactic acid specimens using Taguchi design of experiment method. *J Thermoplast Compos Mater*. 2020;35(12):2435-2452.

    doi: 10.1177/0892705720964560

14. Kumar MS, Farooq MU, Ross NS, Yang CH, Kavimani V, Adediran AA. Achieving effective interlayer bonding of PLA parts during the material extrusion process with enhanced mechanical properties. *Sci Rep.* 2023;13(1):6800.

    doi: 10.1038/s41598-023-33510-7

15. Ramadan S, Altwarah Q, Abu-Shams M, Alkurdi D. Optimizing tensile strength and energy consumption for FDM through mixed-integer nonlinear multi-objective optimization and design of experiments. *Heliyon*. 2024;10(9):e30164.

    doi: 10.1016/J.HELIYON.2024.E30164

16. Panico A, Corvi A, Collini L, Sciancalepore C. Multi objective optimization of FDM 3D printing parameters set via design of experiments and machine learning algorithms. *Sci Rep.* 2025;15(1):16753.

    doi: 10.1038/s41598-025-01016-z

17. Medibew T. A comprehensive review on the optimization of the fused deposition modeling process parameter for better tensile strength of PLA-printed parts. *Adv Mater Sci Eng*. 2022;2022:1-11.

    doi: 10.1155/2022/5490831

18. Hamid RA, Husni S, Ito T. Effect of printing orientation and layer thickness on microstructure and mechanical properties of PLA parts. *Malays J Compos Sci Manuf*. 2022;8:11-23.

    doi: 10.37934/mjcsm.8.1.1123

19. Ahmed NA, Page JR. Manufacture of an unmanned aerial vehicle (UAV) for advanced project design using 3D printing technology. *Appl Mech Mater*. 2013;397-400:970-980.

    doi: 10.4028/www.scientific.net/AMM.397-400.970

20. Kantaros A, Drosos C, Papoutsidakis M, Pallis E, Ganetsos T. Composite filament materials for 3D-printed drone parts: Advancements in mechanical strength, weight optimization and embedded electronics. *Materials (Basel)*. 2025;18(11):2465.

    doi: 10.3390/ma18112465

21. Goh GD, Agarwala S, Goh GL, Dikshit V, Sing SL, Yeong WY. Additive manufacturing in unmanned aerial vehicles (UAVs): Challenges and potential. *Aerosp Sci Technol*. 2017;63:140-151.

    doi: 10.1016/J.AST.2016.12.019

22. Huang Y, Tian X, Li W, *et al.* 3D printing of topologically optimized wing spar with continuous carbon fiber reinforced composites. *Compos B Eng*. 2024;272:111166.

    doi: 10.1016/J.COMPOSITESB.2023.111166

23. Goh GD, Toh W, Yap YL, Ng TY, Yeong WY. Additively manufactured continuous carbon fiber-reinforced thermoplastic for topology optimized unmanned aerial vehicle structures. *Compos B Eng*. 2021;216:108840.

    doi: 10.1016/J.COMPOSITESB.2021.108840

24. Syed B, Rhaman Q, Shahriar H, Khan MMA. *Grey-Taguchi Approach for Optimizing Fused Deposition Modeling Process in Terms of Mechanical Properties and Dimensional Accuracy*. In: *Conference: International Conference on Engineering Research and Education School of Applied Science and Technology,* SUST, Sylhet; 2021.

25. Kumar K, Singh H. Multi-objective optimization of fused deposition modeling for mechanical properties of biopolymer parts using the grey-taguchi method. *Chinese J Mech Eng*. 2023;36(1):30.

    doi: 10.1186/s10033-023-00847-z

26. Chinchanikar S, Shinde S, Shaikh A, Gaikwad V, Ambhore NH. Multi-objective Optimization of FDM using hybrid genetic algorithm-based multi-criteria decision-making (MCDM) techniques. *J Institut Eng Ser D*. 2024;105(1):49-63.

    doi: 10.1007/s40033-023-00459-w

27. Kaptan A, Kartal F. A critical review of composite filaments for fused deposition modeling: Material properties, applications, and future directions. *Eur Mech Sci*. 2024;8:199-209.

    doi: 10.26701/ems.1451829